Protective role of mitophagy on microglia-mediated neuroinflammatory injury through mtDNA-STING signaling in manganese-induced parkinsonism

Yang Lu[1†], Liang Gao[1,2†], Yuqing Yang[1], Dihang Shi[1], Zhipeng Zhang[1], Xiaobai Wang[1], Ying Huang[1], Jie Wu[1],
Jia Meng[1,2], Hong Li[1,2] and Dongying Yan[1,2*]

Abstract

Manganese (Mn), the third most abundant transition metal in the earth's crust, has widespread applications in the emerging field of organometallic catalysis and traditional industries. Excessive Mn exposure causes neurological syndrome resembling Parkinson's disease (PD). The pathogenesis of PD is thought to involve microglia-mediated neuroinflammatory injury, with mitochondrial dysfunction playing a role in aberrant microglial activation. In the early stages of PD, PINK1/Parkin-mediated mitophagy contributes to the microglial inflammatory response via the cGAS/STING signaling pathway. Suppression of PINK1/Parkin-mediated mitophagy due to excessive Mn exposure exacerbates neuronal injury. Moreover, excessive Mn exposure leads to neuroinflammatory damage via the microglial cGAS-STING pathway. However, the precise role of microglial mitophagy in modulating neuroinflammation in Mn-induced parkinsonism and its underlying molecular mechanism remains unclear. Here, we observed that Mn-exposed mice exhibited neurobehavioral abnormalities and detrimental microglial activation, along with increased apoptosis of nerve cells, proinflammatory cytokines, and intracellular ROS. Furthermore, in vivo and in vitro experiments showed that excessive Mn exposure resulted in microglial mitochondrial dysfunction, manifested by increased mitochondrial ROS, decreased mitochondrial mass, and membrane potential. Additionally, with the escalating Mn dose, PINK1/Parkin-mediated mitophagy changed from activation to suppression. This was evidenced by decreased levels of LC3-II, PINK1, p-Parkin/Parkin, and increased levels of p62 protein expression level, as well as the colocalization between ATPB and LC3B due to excessive Mn exposure. Upregulation of mitophagy by urolithin A could mitigate Mn-induced mitochondrial dysfunction, as indicated by decreased mitochondrial ROS, increased mitochondrial mass, and membrane potential, along with improvements in neurobehavioral deficits and attenuated detrimental microglial activation. Using single-nucleus RNA-sequencing (snRNA-seq) analysis in the Mn-exposed mouse model, we identified the microglial cGAS-STING signaling pathway as a potential mechanism underlying Mn-induced neuroinflammation. This pathway is associated with an increase in cytosolic mtDNA levels,

---

†Yang Lu and Liang Gao contributed equally to this work.
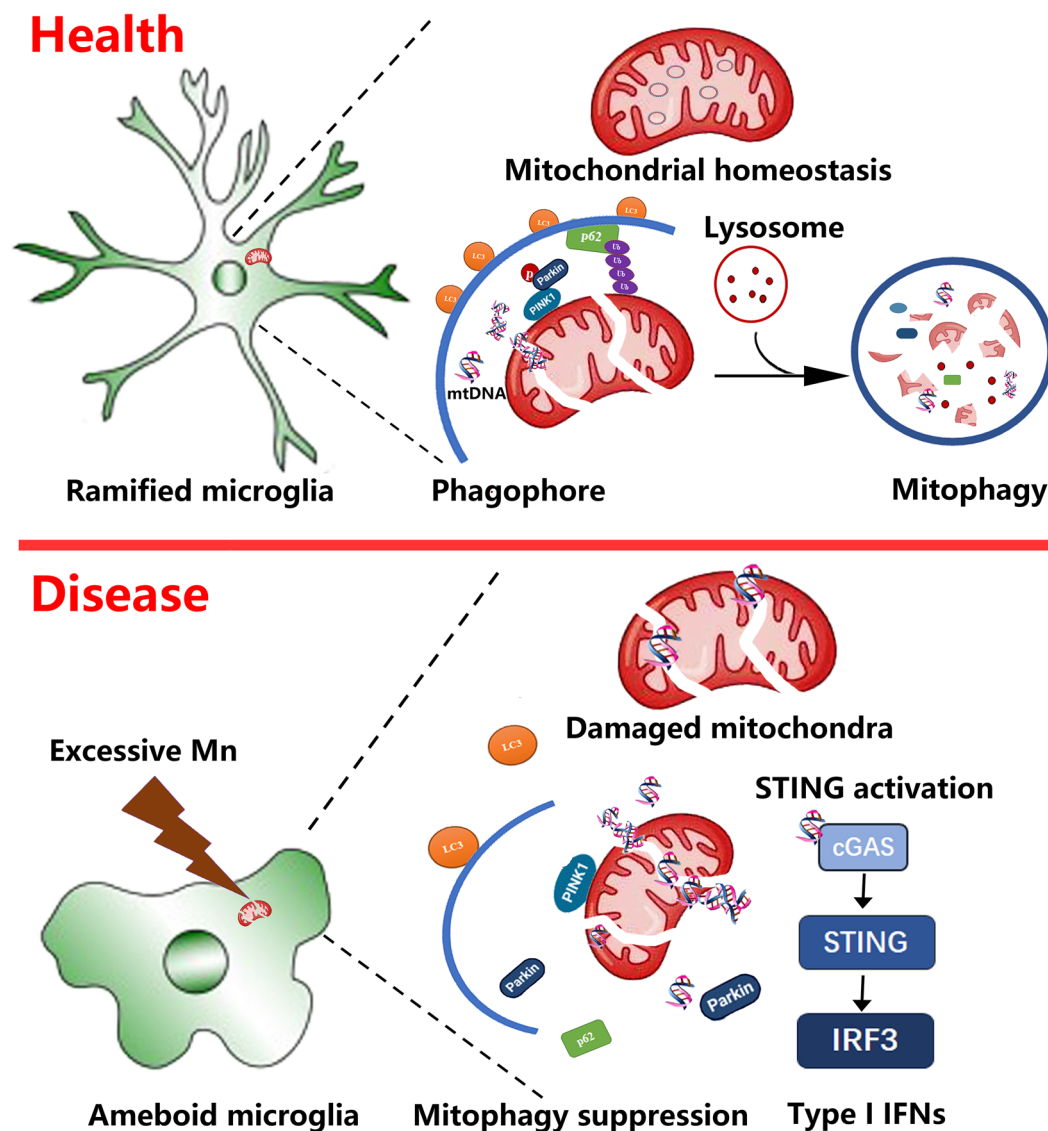
*Correspondence:
Dongying Yan
yandongying@jzmu.edu.cn

Full list of author information is available at the end of the article

which activate STING signaling. These findings point to the induction of microglial mitophagy as a viable strategy to alleviate Mn-induced neuroinflammation through mtDNA-STING signaling.

Graphical Abstract

Introduction

Parkinson's disease (PD), the second most prevalent neurodegenerative disorder, is characterized by the degeneration of dopaminergic (DA) neurons in the substantia nigra, leading to motor impairments such as bradykinesia, tremor, rigidity, and various non-motor symptoms [1]. The global prevalence of PD is on a rapid rise, with estimates exceeding 6 million cases [2, 3]. The environmental pollutant manganese (Mn) has been recognized as a risk factor for sporadic PD and other neurodegenerative diseases [4, 5]. Since the initial documentation of Mn-induced parkinsonism in 1837, numerous experimental and epidemiological studies have been conducted to elucidate this association [6–11]. Notably, in Mn-induced Parkinsonism, dopaminergic neuronal loss in the substantia nigra is minimal, whereas toxicity predominantly affects medium spiny neurons in the striatum. This pathological pattern diverges from idiopathic Parkinson's disease (PD), which is distinguished by significant dopaminergic neuron degeneration in the substantia nigra pars compacta, progressive deterioration of nigrostriatal connections, Lewy body formation, and preservation of

Lu *et al. Journal of Neuroinflammation*   (2025) 22:55

Page 3 of 20

the pallidum [4, 6, 12]. As the third most abundant transition metal in the earth's crust, Mn is extensively utilized in diverse applications, including as an additive in gasoline (methylcyclopentadienyl manganese tricarbonyl), pesticides (manganese ethylene-bis-dithiocarbamate), an adjuvant in medical imaging and antineoplastic therapy (manganese porphyrins), in drug addicts (potassium permanganate), as manganese violet in paints and cosmetics, and in lithium manganate batteries [13–15]. This has led to an increasing public awareness concerning the neurotoxic repercussions linked to Mn exposure.

Mn is a vital trace element essential for regulating key physiological processes such as amino acid and lipid metabolism, protein synthesis, neurotransmitter synthesis, and immune function [16]. However, excessive exposure to Mn can have toxic effects on humans, with notable accumulation in the globus pallidus, striatum, substantia nigra, and frontal cortex occurring through facilitated diffusion, active transport across the blood-brain barrier, or passive transport, ultimately causing irreversible damage to dopaminergic neurons [16–18]. Apart from Parkinson's-like disease, increasing evidence reveals that Mn may also be a risk factor for several other neurodegenerative disorders, including Alzheimer's disease (AD), dementia, amyotrophic lateral sclerosis (ALS), and Huntington's disease (HD), depression [10, 18]. Mn neurotoxicity involves multiple mechanisms, including mitochondrial dysfunction, disruption of neurotransmitter metabolism, oxidative stress, neuroinflammation, iron imbalance, and proteotoxicity [6, 18]. Developing effective intervention strategies to prevent Mn-related neurological disorders remains an urgent research priority. Neuroinflammation is considered a pivotal mediator in the mechanism underlying the neurodegenerative process [6, 19–22]. Recent findings have observed a detrimental inflammation in response to Mn overexposure and related disorders, accompanied by elevated inflammatory cytokines such as TNF-α, iNOS, and IL-6, which contribute to its neurotoxic effects [21–23]. Multiple compromised homeostatic mechanisms can independently contribute to nerve cell damage, ultimately converging to produce an aberrant inflammatory state that drives neurodegeneration [6, 21, 24–26]. The attenuation of microglia-mediated inflammation has emerged as a common mechanism through which interventions, including pharmacological ones, exert beneficial effects on neurodegenerative processes.

Microglia, an important component of the innate immune system in the central nervous system (CNS), respond to a broad range of pathogen-associated and danger-associated molecular patterns (DAMPs) [19]. Microglial immune response is also known to be controlled by mitochondrial homeostasis. Mitochondria-derived DAMP molecules, such as ROS and DNA,

contribute to the perpetuation of neuroinflammation by sustaining microglial activation and causing neurotoxic damage in the neuropathology of PD and other neurodegenerative diseases [20, 27]. The mitochondria are the primary organelle responsible for the accumulation of Mn via mitochondrial Ca^{2+} uniporter [6]. Excessive exposure to Mn increases ROS and mitochondrial ROS (mtROS) production, inhibits ATP production, and perturbs mitochondrial quality control, exacerbating the oxidative stress and nerve cell damage [28–30]. However, the exact mechanisms of Mn-induced mitochondrial dysfunction in microglial function and activation remain unclear and need to be investigated.

Malfunctioning mitochondria have been implicated in several neurodegenerative diseases such as Alzheimer's disease (AD) and PD [1, 31–34]. Mitophagy pathways play a crucial role in maintaining cellular homeostasis by degrading defective or damaged mitochondria [35]. Dysregulation of mitophagy is associated with various pathological processes, including neuroinflammation, apoptosis, and cell differentiation, which can exacerbate AD and PD [35, 36]. Emerging evidence suggests that the PTEN-induced putative kinase 1 (PINK1)/parkin RBR E3 ubiquitin-protein ligase (Parkin)-mediated mitophagy pathway regulates the microglial inflammatory response through the mtDNA/cyclic GMP-AMP synthase (cGAS)-interferon gene stimulator (STING/TMEM173) signaling, contributing to the progression of early-onset PD [37]. In terms of innate immune responses, Mn has been considered as the second cGAS activator, apart from exogenous double-stranded DNA, to activate the cGAS-STING pathway for potential therapeutic interventions in infectious diseases and malignant tumors [38–40]. In regards to neurotoxicity, recent studies have shown that Mn exposure induces neuronal mitochondrial dysfunction by impairing mitochondrial biogenesis and repressing PINK1/Parkin-mediated mitophagy, exacerbating nerve cell damage [28, 30]. Additionally, excessive Mn exposure activates the microglial cGAS-STING pathway, contributing to neuroinflammatory damage [22]. However, the role of microglial mitophagy in Mn-induced neuroinflammation and its potential involvement in the mtDNA-STING pathway requires further investigation.

In this study, we conducted in vivo and in vitro experiments to investigate the impact of Mn on microglial mitophagy and neuroinflammation. We utilized the mitophagy activator, urolithin A (UA), to assess the neuroprotective effects of microglial mitophagy in Mn-induced neuroinflammation. By employing single-nucleus RNA sequencing (scRNA-seq) technology, we elucidated the molecular mechanism by which microglial mitophagy regulates neuroinflammation through the mtDNA-STING pathway under Mn neurotoxic

conditions. Our findings offer novel insights into the understanding of Mn neurotoxicity.

Materials and methods

Antibodies and reagents

$MnCl_2 \cdot 4 H_2O$ was acquired from Sigma Chemical Co. (St. Louis, MO, USA). Urolithin A (UA) was purchased from MedChemExpress (HY-100599). Dulbecco's modified Eagle medium (DMEM) and fetal bovine serum (FBS) were purchased from Gibco (Grand Island, USA). Primary antibodies, including Rabbit anti-p62 (#A11247), anti-LC3B (#A7198), anti-IBA1 (#A19776), and anti-β-actin (#AC026), along with secondary antibodies, were purchased from Abclonal Biotechnology Co. Ltd. (Shanghai, China). Rabbit anti-phospho-STING (#72971S), anti-STING (#13647), anti-phospho-IRF3 (#29047), anti-IRF3 (#4302S), anti-phospho-TBK1 (#5483), anti-TBK1 (#3504S), Vinculin (#13901) and VDAC (#4661) were purchased from Cell Signaling Technology (Beverly, MA, USA). Rabbit anti-phospho-Parkin (#PA5-114616), anti-Parkin (#702785), and anti-PINK1 (#PA1-16604) were purchased from Invitrogen Co. Ltd. (Jiangsu, China). Anti-ATPB antibody (#ab14730) was purchased from Abcam. Anti-DNA mouse monoclonal antibody (#690014) was obtained from Progen biotechnology Inc (Heidelberg, Germany). Bicinchoninic acid reagent (BCA, #23227), Reactive Oxygen Species Assay Kit (#S0033M), Mitochondrial membrane potential assay kit with JC-1 (#C2006), Enhanced ATP Assay Kit (#S0027), TUNEL Apoptosis Assay Kit (#C1098), Mito-Tracker Green (#C1048), and Mitochondrial Superoxide Assay Kit with MitoSOX Red (S0061M) were purchased from Beyotime Biotechnology (China). Nonyl acridine orange (NAO) was obtained from Sigma-Aldrich (#A7847, USA). ELISA kits were purchased from Shanghai Enzyme-linked Biotechnology Co., Ltd (Shanghai, China). DNA Isolation Mini Kit-BOX (Cat.DC102-01) and ChamQ Universal SYBR qPCR Master Mix (Code. Q711-02) were purchased from Vazyme Biotech Co., Ltd (Nanjing, China).

Animals and treatments

Eighty male C57BL/6 mice, aged 6–8 weeks and weighing 22–25 g, were procured from Beijing Vital River Laboratory Animal Technology Co., Ltd. Following a one-week acclimatization period in a controlled environment with a 12-hour light/dark cycle at 22 ± 2 °C and ad libitum access to food and water, the mice ($n = 10$ per group) were allocated into distinct groups: control (saline solution), varying doses of Mn-exposed groups (50, 100, 200 μmol/kg Mn), a UA control group (2.3 mg/kg UA), and a UA-pretreated group (2.3 mg/kg UA + 200 μmol/kg Mn). The Mn and UA dosages and administration methods adhered to established protocols [23, 29, 41–43].

Mn-exposed mice received intraperitoneal Mn injections for 5 consecutive days per week, while UA-pretreated mice were administered UA intraperitoneally 2 h prior to Mn treatment for 3 consecutive days within the same timeframe. Regular neurobehavioral assessments were conducted to monitor changes in locomotor function. Striatal tissue samples were collected to evaluate relevant indicators until 80% of Mn-treated mice displayed abnormal neurobehavioral performance six weeks post-Mn exposure. The in vivo experimental schedule is detailed in Supplementary Material Figure S1. The experimental procedures and ethical considerations were approved by the Animal Research Committee at Jinzhou Medical University in Jinzhou, China under ethical approval number 240,079.

BV2 cell culture

BV2 murine microglial cells were cultured in DMEM supplemented with 10% fetal bovine serum (FBS) and 1% penicillin/streptomycin in T25 flasks at 37 °C with 5% CO_2 until reaching 90% confluency. The study comprised two phases: initially, cells were exposed to varying concentrations of Mn (0, 200, 400, and 600 μM) for 24 h. Subsequently, cells were treated with either 600 μM Mn alone or pre-treated with 10 μM UA for 2 h followed by Mn exposure according to the previous reports [23, 44, 45]. After 24 h of co-culture, relevant parameters were assessed.

Gait analysis

Each mouse traversed the glass walkway three times, while a high-speed camera captured their footprints. Parameters including such as footprint timing, footfall patterns, stance(s), stride length(cm), and step cycle(s) were automatically documented utilizing the Catwalk Gait Analysis System (VisuGait, XR-XFP101, Shanghai).

Open-field test

Each mouse was placed directly into the middle of the white floor of the apparatus (50 cm × 50 cm × 40 cm). The movement of each mouse within 5 min was recorded with a high-speed camera. During the trial, the open field device was wiped with 75% alcohol to remove odor cues. Parameters including total distance, average velocity, and immobility time were automatically calculated using Tracking Master software.

Mn content assessment

Approximately 25 mg of striatal tissue was pretreated with 5 mL digestion solution (HNO_3: 30% H_2O_2 = 4:1). After the sample was completely dissolved by programmed heating, heated to evaporate to the last drop. Subsequently, deionized water was added to 6 mL. A standard curve of Mn was made to quantify the

Lu *et al. Journal of Neuroinflammation*   (2025) 22:55

Page 5 of 20

concentration of Mn in different striatal tissues using ICP-MS (SUPEC 7000, Hangzhou). Data were analyzed by calculation of µg Mn/ g tissue wet weight.

Enzyme-linked immunosorbent assay (ELISA) assay
Levels of TNF-α, IFN-γ, iNOS, and IL-6 in the supernatant of fresh striatal tissue were detected using ELISA kits following the manufacturer's instructions. The absorbance at 450 nm was measured on a microplate reader respectively. The total protein concentrations were determined for standardized analysis. The contents of TNF-α, IFN-γ, iNOS, and IL-6 were normalized by the total protein.

Terminal Deoxynucleotidyl Transferase-mediated dUTP Nick-End labeling (TUNEL) assay
Brain tissue paraffin Sect. (5 µm-thick) were deparaffinized in xylene and hydrated through graded concentrations of ethanol. The fragmented DNA was labeled on the sections using components of the Colorimetric TUNEL Apoptosis Assay Kit according to the supplier's instructions kit. Then the brain sections were counterstained by immersing the slides in hematoxylin. Photos were taken by microscopy and analyzed by Image J.

Immunohistochemical (IHC) analysis
Brain tissue paraffin sections (5 µm thick) were deparaffinized in xylene, hydrated in a series of ethanol concentrations, and subjected to antigen retrieval in citrate buffer using a microwave pressure cooker. Following cooling to room temperature, the sections underwent blocking for endogenous peroxidase and nonspecific binding, then were incubated with the primary antibody IBA-1 (1: 200) overnight at 4 ℃. Subsequently, the sections were treated with anti-rabbit IgG for 2 h at 37 ℃, followed by staining with 3,3-diaminobenzidine (DAB) for 5 min. After dehydration in ethanol, the sections were mounted with neutral gum. Microscopic images were captured and analyzed using Image J.

Flow cytometry
Single-cell suspension of striatum tissue were prepared as previously described and incubated with DCFH-DA, MitoSOX™, nonyl acridine orange (NAO) or JC-1 dye. The specific staining working concentration and condition were performed according to the instructions of reactive oxygen species (ROS) assay kit, mitochondrial superoxide (mtROS) assay kit, mitochondrial mass assay, and mitochondrial membrane potential (MMP) assay kit. Cell suspensions were analyzed using a flow cytometer (EasyCell, Wellgrow Technology, China), and data were analyzed using FlowJo software.

Immunofluorescence analysis
Fixed BV2 cells, mouse brain paraffin Sect. (5-µm thick) were permeabilized with 0.1% Triton X-100 and incubated with 5% goat serum albumin for 30 min to block a nonspecific binding. Samples then were incubated with mouse ATPB (1:200), rabbit LC3B (1:200), or mouse DNA primary antibodies overnight at 4 ℃. Cy3-labeled or FITC-labeled fluorescent secondary antibodies (#A0516, #A0568, Beyotime) were used to immunostain before mounting in fluoroshield with DAPI (#P0131, Beyotime). For the detection of mtROS, BV2 cells were co-incubated with Mito-Tracker Green probe and MitoSOX Red probe at 37 ℃ for 20 min in the dark. For the detection of MMP, BV2 cells were stained with the JC-1 probe at 37 ℃ for 20 min in the dark using an MMP assay kit. The fluorescence signal image was captured by confocal microscopy and analyzed by Image J.

ATP assay
The ATP concentration in BV2 cells was measured using the Enhanced ATP Assay Kit according to the manufacturer's protocol. The luminescent signal was detected by an Enzyme-linked immunoassay analyzer (Feyond-A300, ALLSHENG, China).

Western blotting analysis
Striatum tissues or BV2 cells were dissolved in RIPA buffer with 1% PMSF. Total proteins were determined and quantified at 2 µg/µl using BCA assay. Equal quantities of protein were separated by SDS-PAGE gels and subsequently transferred to PVDF membranes. After blocking the PVDF membrane with 5% BSA for 2 h at room temperature, the membranes were probed with the primary antibodies including Parkin, p-Parkin, LC3B, p62, PINK1, STING, p-STING, TBK-1, p-TBK-1, IRF-3 (1:1000), p-IRF-3, VDAC, Vinculin, and β-actin at 4 ℃ overnight. Membranes were incubated with rabbit secondary antibody for 2 h, and the expression of target bands was visualized using the ECL chemiluminescent system. Finally, the relative protein expression level was assessed by Image J software to measure the band integrated density.

Mitochondrial DNA copy number (mtDNA) measurement
Genomic DNA was isolated from BV2 cells using the DNA Isolation Mini Kit (Cat.DC102-01, Vazyme). The mtDNA was detected by quantitative PCR (qPCR) to determine the mitochondrial DNA marker *Cox1* /nuclear DNA marker *Ndufv1* ratio. The qPCR was performed using SYBR green dye (Code.Q711-02, Vazyme) in the ABI 7500 qPCR system (Applied Biosystems). The following primer sequences were used: *Cox1*: 5′-TGC TAG CCG CAG CAT TAC-3′ (forward), 5′-GGG TGC CCA AAG AAT CAG AAC-3′ (reverse); *Ndufv1*: 5′-CTT CCC CAC TGG CCT CAA G-3′ (forward), 5′-CCA AAA CCC

Lu *et al. Journal of Neuroinflammation*   (2025) 22:55

Page 6 of 20

AGT GAT CCA GC-3′ (reverse). The data were normalized and analyzed using the $2^{-\Delta\Delta Ct}$ method.

Single-nucleus RNA-sequencing (snRNA-seq) and bioinformatic analysis

SnRNA-seq was conducted by Scale Biomedicine Technology Co., LTD (Beijing, China). After preparing cell nucleus suspensions from fresh striatal tissue samples of Mn-treated mice and control mice, nuclear capture and cDNA library amplification were performed according to the operating manual of the 10× Genomics Chromium Next GEM Single Cell 3′ Reagent Kits v3.1 (1000268). The 10× Genomics Chromium Library Construction Kit (1000190) was then used for library construction, following the operating manual.

Raw sequencing data generated from the single-cell RNA sequencing experiment were first processed using Cell Ranger (v7.0.0) provided by 10x Genomics. Cell Ranger was employed to demultiplex the sequencing reads, align them to the reference genome (mm10 for mouse), and generate a gene-barcode matrix. The matrix contains the UMI (Unique Molecular Identifier) counts per gene for each cell.

After obtaining the gene expression matrix, the data were imported into Seurat (v4.3.0) for further analysis [46]. To ensure high-quality single-cell data for downstream analysis, stringent filtering criteria was applied to remove low quality cells and doublets. To filter out cells with an extremely high or low number of detected genes or UMI counts, the nFeature_RNA and nCount_RNA metrics, representing the number of expressed genes and the total UMI counts per cell, were filtered to retain only those cells within the 2.5th to 97.5th percentile range. Cells with over 10% mitochondrial gene expression (percent. mt > 10%) were considered as dead or dying cells and were filtered out. Additionally, the DoubletFinder package (version 2.0.3) was applied to identify potential doublets [47].

After applying these QC criteria, individual datasets were merged using the merge function. The combined object was normalized using the NormalizeData function with the LogNormalize method and a scale factor of 10,000. Two thousand highly variable genes were identified using the FindVariableFeatures function with the variance-stabilizing transformation (VST) method. The data was scaled using the ScaleData function with default parameters. Principal component analysis (PCA) was performed with the RunPCA function to reduce dimensionality. The first several PCs (40) were selected based on their contribution to the variance in the dataset, evaluated through an elbow plot or JackStraw plot. To address batch effects, the Harmony algorithm was applied using the RunHarmony function [48]. After batch correction, a neighbor graph of the cells was constructed using the FindNeighbors function with the first (40) principal components. Clustering was then performed using the FindClusters function to partition the cells into distinct groups, with the resolution parameter set to 0.5 adjusted to control the granularity of clustering. Non-linear dimensionality reduction was conducted using uniform manifold approximation and projection (UMAP) and t-distributed stochastic neighbor embedding (t-SNE) by applying RunUMAP and RunTSNE on the Harmony-aligned components, focusing on the first (40) principal components.

To assign cell type labels to each cluster, marker genes were discerned by contrasting gene expression within clusters against other cells using the FindMarkers function with the Wilcoxon rank sum test. Reference-based cell type annotation was performed using SingleR package (version 1.8.1) [49].

The differentially expressed genes (DEGs) between experimental treatment sample groups were discerned by contrasting gene expression within one sample group against the other group using the FindMarkers function with the Wilcoxon rank sum test method. To explore functional enrichment of DEGs, the Gene Set Enrichment Analysis (GSEA) was conducted by the clusterProfiler package (version 4.8.0) [50]. Utilizing the genes of the cGAS-STING signaling pathway in the KEGG database as gene sets, the cGAS-STING activity score was calculated by the Viper algorithm (version 1.38.0) in the irGSEA package (version 3.3.2) [51]. ISG analysis and interferon type classification were conducted using Interferome 2.0 [52]. All analyses and visualizations were conducted using R (version 4.4.1).

Statistical analysis

All statistical tests were performed with SPSS 25.0 software (SPSS Co. Ltd, Aromonk, NY, USA). Data represent the mean of at least three independent experiments, and error bars denote the standard deviation unless specified otherwise. If data conformed to normality and variance homogeneity, significance was performed by a one-way ANOVA followed by the SNK-q test for multiple comparisons. The difference was considered statistically significant at $P < 0.05$.

Results

Mn overexpose induced abnormal neurobehavioral performance and neuroinflammation damage in mice

Following Mn treatment, catwalk gait analysis and open field tests were conducted to evaluate the impact of Mn neurotoxicity in mice. Mn-treated mice exhibited irregular swinging cycles, abnormal step sequences, and impaired gait performance compared to the control group, as evidenced by increased stand time and step cycle, and decreased stride length (Fig. 1A and B). In

Fig. 1 (See legend on next page.)

Lu *et al. Journal of Neuroinflammation*   (2025) 22:55

Page 8 of 20
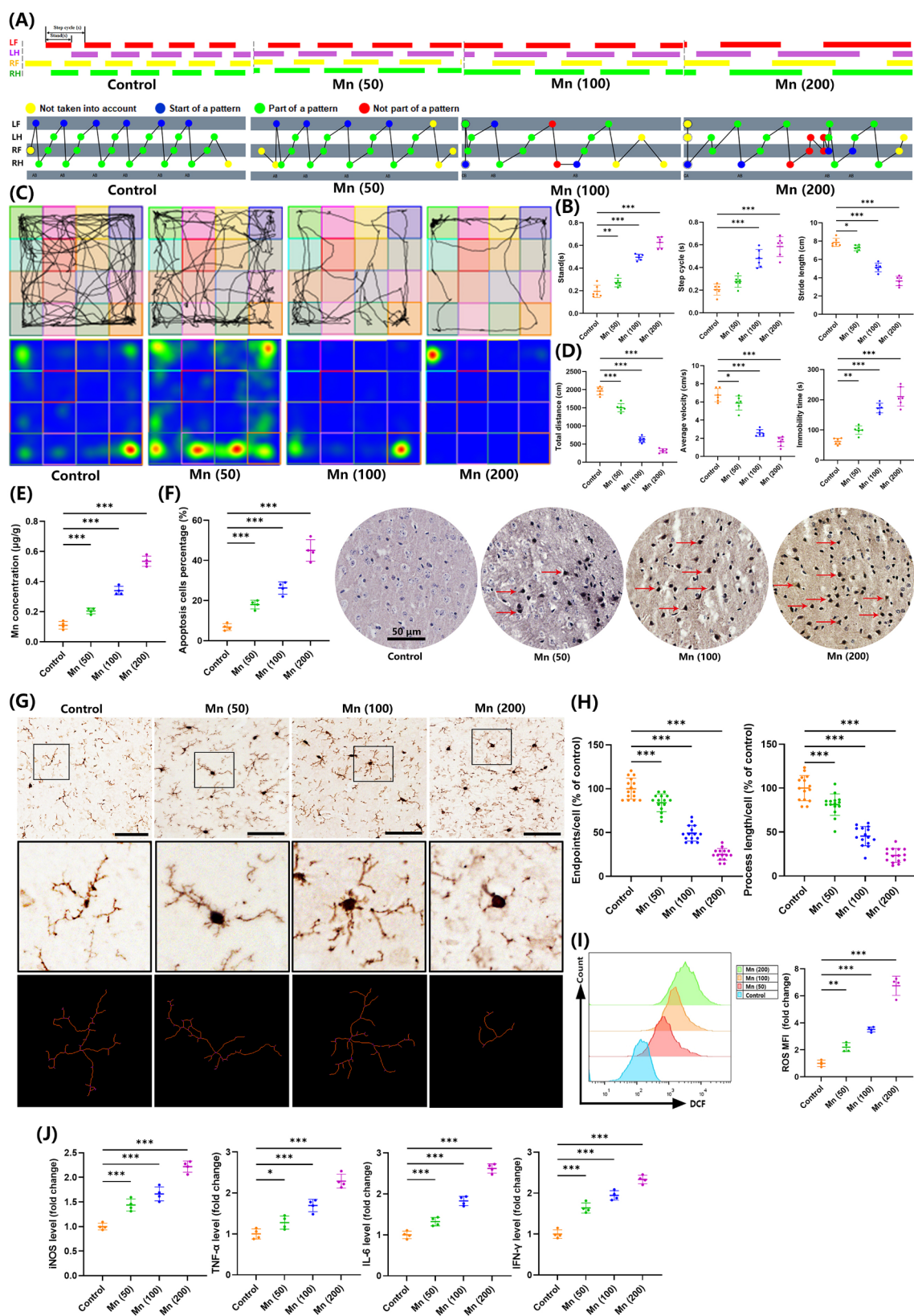
(See figure on previous page.)

Fig. 1 Excessive Mn exposure induces neurobehavioral impairments and microglial activation. (**A, B**) Catwalk gait analysis reveals impaired motor coordination in Mn-treated mice, as indicated by increased stand time and step cycle and decreased stride length ($n = 6$ mice). (**C, D**) The open-field test shows reduced locomotor activity, as evidenced by reduced total distance, velocity, and increased immobility time ($n = 6$ mice). (**E**) Mn accumulation in the striatum was dose-dependent, and quantified by ICP-MS ($n = 4$ mice). (**F**) TUNEL assay demonstrates increased nerve cell apoptosis in the Mn-treated group ($n = 4$ mice). (**G, H**) Iba-1 immunostaining reveals amoeboid microglial morphology in Mn-treated mice, with shorter branches and fewer endpoints ($n = 3$ mice). (I) Flow cytometry shows elevated ROS levels in the striatum ($n = 4$ mice). (J) ELISA results indicate increased inflammatory cytokines (iNOS, TNF-α, IL-6, IFN-γ) in Mn-treated mice ($n = 4$ mice). Data are presented as mean ± SD; significance is denoted as $^*P < 0.05$, $^{**}P < 0.01$, $^{***}P < 0.001$

the open field tests, a gradual decrease in total distance and average velocity, along with an increase in immobility time, was observed with higher Mn concentrations (Fig. 1C and D). The accumulation of Mn in the striatum region also increased with elevated Mn exposure doses (Fig. 1E). Pathological changes in nerve cells in the striatum region of Mn-treated mice were observed, with the TUNEL assay revealing a significant increase in nerve cell apoptosis with higher Mn concentrations (Fig. 1F). Immunohistochemical analysis showed morphological alterations in microglia labeled by Iba-1, characterized by enlarged cell bodies and shortened branches, displaying a decrease in endpoints and process length in the Mn-treated group compared to the control group (Fig. 1G and H). Flow cytometry results demonstrated varying levels of increased intracellular reactive oxygen species (ROS) following Mn exposure (Fig. 1I). ELISA assay findings indicated a substantial increase in the expression of inflammatory cytokines (iNOS, TNF-α, IL-6, and IFN-γ) due to Mn exposure (Fig. 1J). These results suggested that microglia-mediated neuroinflammatory damage may play a significant role in the neurobehavioral dysfunction induced by Mn exposure.

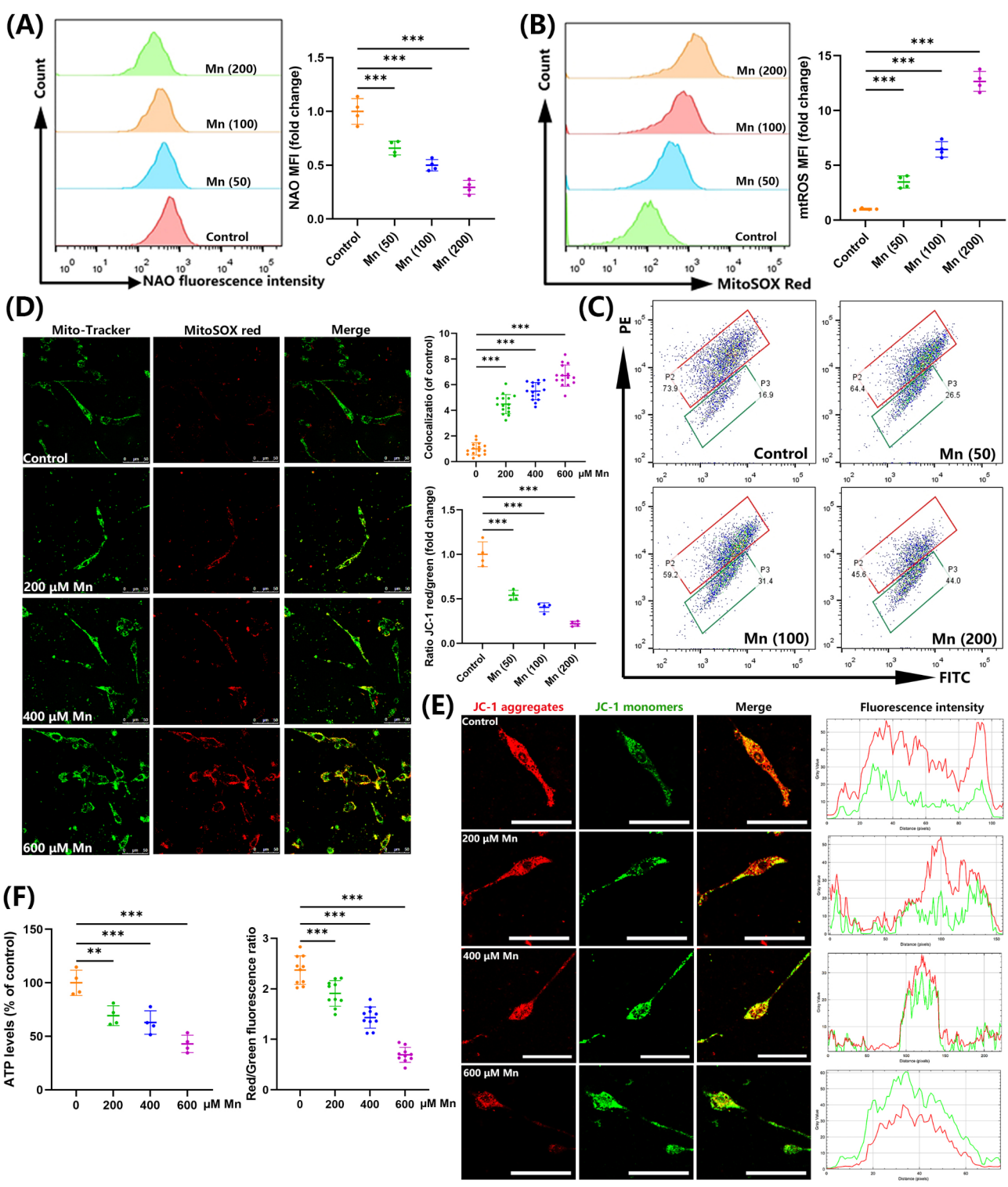## Mn overexposure impairs microglial mitochondrial function in vivo and in vitro

Mitochondria play a critical role in the pathogenesis of Parkinson's disease (PD), with mitochondrial dysfunction closely associated with neuroinflammatory damage. To investigate the impact of Mn on mitochondrial function, we evaluated mitochondrial mass, mitochondrial ROS levels, and mitochondrial membrane potential (MMP) in the striatum of Mn-treated mice. Flow cytometry analysis using NAO dye demonstrated a significant decrease in mitochondrial mass following Mn exposure (Fig. 2A). Furthermore, Mn exposure increased mtROS levels (Fig. 2B). The flow cytometry assay revealed a significant reduction in MMP after Mn exposure, as evidenced by the decreased ratio of JC-1 aggregated formation (red fluorescent signal) to JC-1 monomer formation (green fluorescent signal) (Fig. 2C). To explore the connection between mitochondrial function and microglia-mediated neuroinflammation in response to Mn exposure, we also assessed the mtROS and MMP levels in BV2 cells treated with an Mn dose of 200–600 μM. This dose was chosen based on our previous findings that inflammatory activation of BV2 cells contributes to Mn-induced

neuroinflammatory damage [23]. Immunofluorescence analysis showed a significant increase in mtROS levels in Mn-treated BV2 cells compared to the control group (Fig. 2D). Furthermore, JC-1 staining demonstrated a decrease in the red/green fluorescent intensity ratio in Mn-treated BV2 cells, indicative of reduced MMP (Fig. 2E). Additionally, the adenosine triphosphate (ATP) levels were significantly lower in Mn-treated BV2 cells than that in the control group (Fig. 2F). These findings suggest that Mn-induced mitochondrial dysfunction may drive microglia-mediated neuroinflammatory damage.

Mn overexposure suppresses microglial mitophagy

Mitophagy is essential for maintaining cellular homeostasis by eliminating damaged or dysfunctional mitochondria, thus preventing the onset of inflammatory responses [33, 41, 53]. In this research, we assessed mitophagy using immunofluorescence staining and western blot methods. Our findings, as shown in Fig. 3A-B, indicate a notable rise in the colocalization between the mitochondrial marker ATPB and the autophagosomal marker LC3B in the brain sections of mice exposed to Mn, suggesting increased mitophagosomes formation following Mn exposure. However, in 200 μmol/kg Mn-treated group, the colocalization signal decreased by 52% compared to the 100 μmol/kg Mn treated group. Corresponding to our in vivo results, the colocalization between ATPB and LC3B in BV2 cells demonstrated a transition from enhancement to reduction with escalating Mn concentrations. Specifically, the BV2 cells treated with 600 μM Mn exhibited a 62% decrease in the colocalization between ATPB and LC3B in comparison to the 400 μM Mn treatment (Fig. 3C and D). We also assessed changes in expression levels of mitophagy-related proteins (PINK1, Parkin, LC3-II, p62) in BV2 cells treated with Mn. The levels of PINK1, p-Parkin/Parkin, and LC3-II proteins increased, while p62 decreased after 200 and 400 μM Mn treatment (Fig. 3E-H), indicating activation of mitophagy in response to Mn-induced aberrant mitochondrial stress. However, it is worth noting that treatment with 600 μM Mn resulted in suppression of mitophagy, as indicated by a decrease in p-Parkin/Parkin and LC3-II protein levels by 37% and 35%, respectively, and a 1.9-fold increase in p62 protein compared to the 400 μM Mn treatment (Fig. 3E-H). These data point towards suppression of microglial mitophagy induced by

Lu *et al. Journal of Neuroinflammation*   (2025) 22:55

Page 9 of 20

Fig. 2 Excessive Mn exposure induces microglial mitochondrial dysfunction. (**A**-**C**) Flow cytometry shows elevated mtROS, reduced mitochondrial mass, and MMP levels in the striatal ($n = 4$ mice). (**D**, **E**) Immunofluorometric analysis reveals elevated mtROS and reduced MMP in Mn-treated BV2 cells ($n = 3$ independent experiments). (**F**) Decreased ATP levels were Mn-dose-dependent in BV2 cells ($n = 4$ independent experiments). MMP was calculated by the ratio of JC-1 red/green. Data are presented as mean ± SD; significance is denoted as $^{**}P < 0.01$, $^{***}P < 0.001$
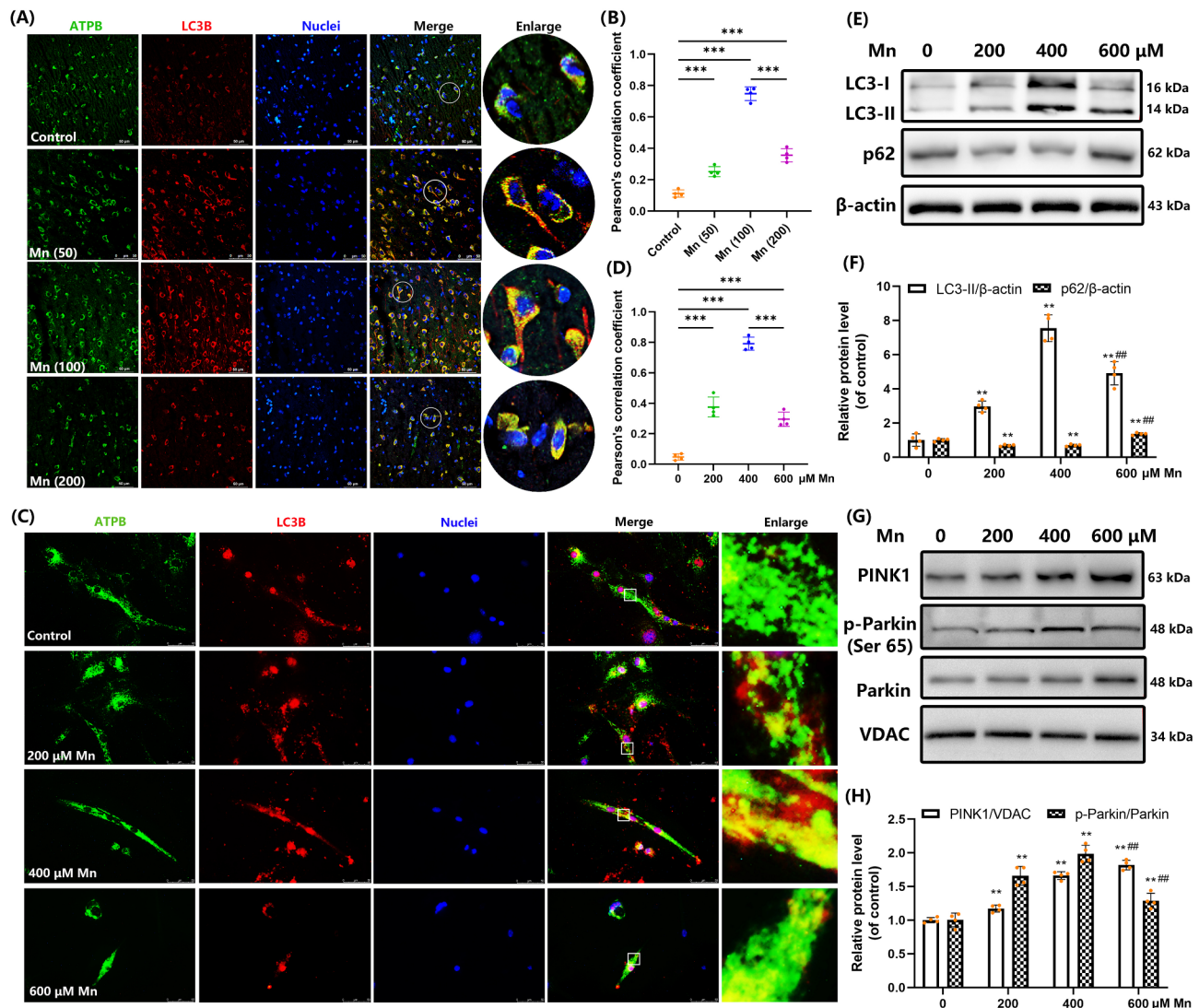
Fig. 3 The effects of Mn on microglial PINK1/Parkin-mediated mitophagy. (**A**, **B**) The ATPB (green) and LC3B (red) colocalization reveals mitophagy from enhancement to reduction in Mn-treated mice brain tissue sections ($n = 4$ mice). (**C**, **D**) The ATPB (green) and LC3B (red) colocalization reveal mitophagy from enhancement to reduction in Mn-treated BV2 cells ($n = 4$ independent experiments). (**E**, **H**) Western blot analysis indicates mitophagy-related mediators (LC3B, p62, PINK1, p-Parkin, and Parkin) dependent on mitophagy levels in Mn-treated BV2 cells ($n = 4$ independent experiments). Protein levels are normalized to the loading control (β-actin or VDAC). Data are presented as mean ± SD; significance is denoted as $^{**}P < 0.01$, $^{***}P < 0.001$ vs. control group; $^{##}P < 0.01$ vs. 400 µM Mn-treated BV2 cells group

excessive Mn exposure, potentially triggering a deleterious inflammatory response.

Pharmacological activation of mitophagy improves mitochondrial dysfunction in response to Mn exposure in vivo and in vitro

To investigate the potential involvement of mitophagy in microglia-mediated neuroinflammatory damage induced by excessive Mn exposure, we conducted an intervention study both in vivo and in vitro using urolithin A (UA) as a mitophagy inducer. UA is a natural metabolite sourced from edible plants and fruits such as pomegranate or raspberries, and is currently under investigation

in clinical trials [44, 54, 55]. Immunofluorescence analysis revealed that pretreatment with UA resulted in a 2.25-fold increase in the colocalization signal between ATPB and LC3B in BV2 cells, in contrast to Mn treatment (Fig. 4A and B). The levels of LC3-II, PINK1, and p-Parkin/Parkin proteins were elevated by 2.12, 1.23, and 1.21-fold, respectively, while there was a 30.4% reduction in p62 protein following UA pretreatment compared to Mn treatment (Fig. 4C-F). Additionally, a 1.81-fold increase in the colocalization signal between ATPB and LC3B was observed in brain sections from UA-pretreated mice compared to the Mn-treated group (Fig. 4G and H). These results suggested that UA pretreatment effectively
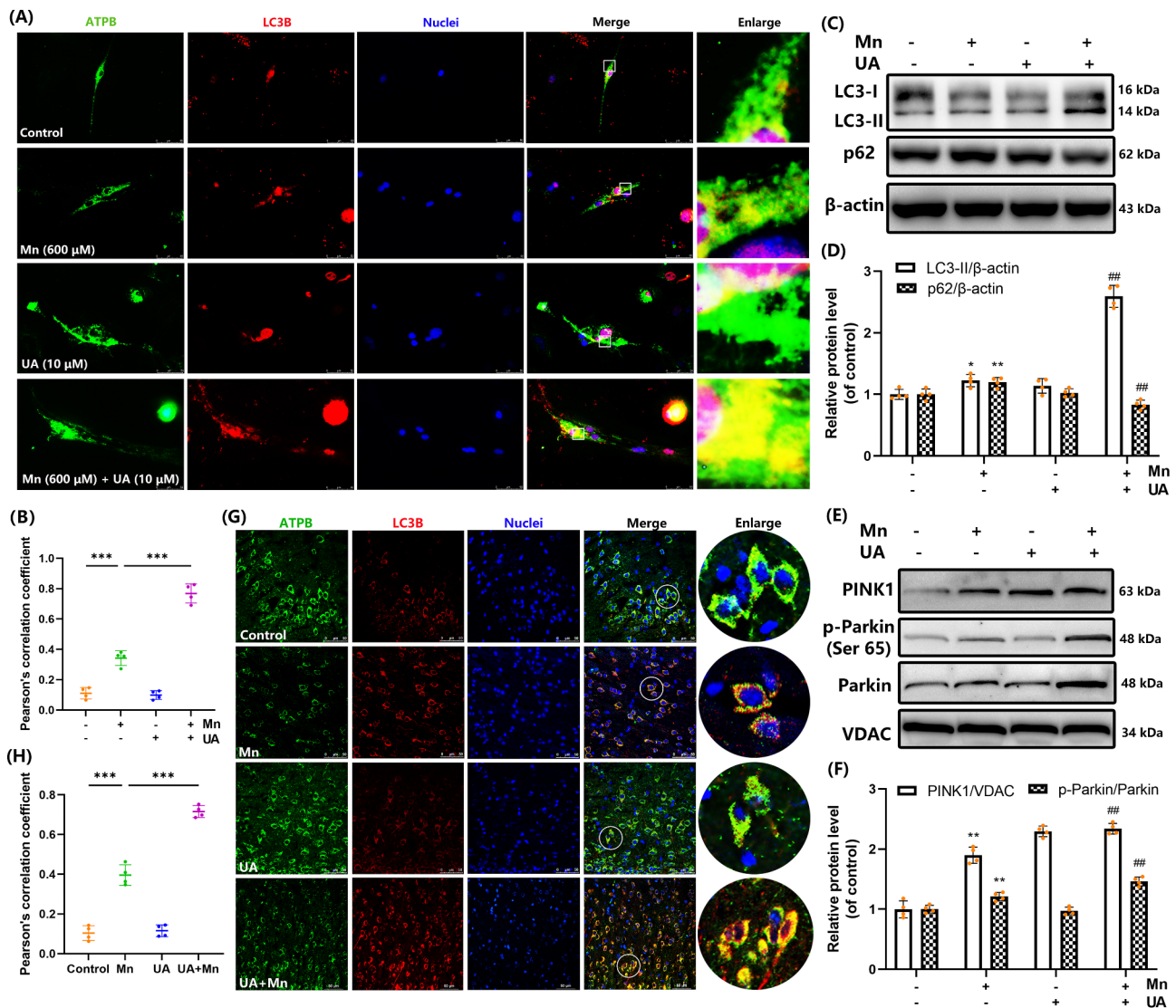
Fig. 4 UA pretreatment ameliorated Mn-induced microglial mitophagy suppression. (**A**, **B**) The ATPB (green) and LC3B (red) colocalization reveal elevated mitophagy in BV2 cells after UA pretreatment ($n = 4$ independent experiments). (**C**-**F**) Western blot analysis indicates mitophagy-related mediators dependent mitophagy levels after UA pretreatment ($n = 4$ independent experiments). (**G**-**H**) The ATPB (green) and LC3B (red) colocalization reveal elevated mitophagy in mouse brain tissue sections after UA pretreatment compared with Mn-treated mice ($n = 4$ mice). Data are presented as mean ± SD; significance is denoted as $^*P < 0.05$, $^{**}P < 0.01$, $^{***}P < 0.001$; $^{**}P < 0.01$ vs. control group; $^{\#\#}P < 0.01$ vs. 600 μM Mn treated-BV2 cells group

upregulated microglial mitophagy activity upon Mn overexposure.

To further elucidate the regulatory role of UA on mitochondrial function, we assessed changes in mitochondrial mass, mtROS levels, and MMP both in vivo and in vitro. Flow cytometry analysis in vivo demonstrated a 1.85-fold increase in mitochondrial mass following UA pretreatment compared to Mn treatment (Fig. 5A). Moreover, mtROS levels were significantly reduced by 57.51% after UA pretreatment in vivo (Fig. 5B). Immunofluorescence staining results in vitro further supported these findings, showing a 45.55% decrease in mtROS levels in UA-pretreated BV2 cells compared to the Mn-treated group (Fig. 5D). Flow cytometry assays

in vivo and immunofluorescence staining in vitro were used to assess JC-1 aggregates and JC-1 monomer signals, reflecting changes in MMP. The results showed that excessive Mn exposure reduced MMP levels, both in vivo and in vitro, but this reduction could be mitigated after UA pretreatment (Fig. 5C and E). Specifically, UA pretreatment resulted in a 1.28 and 2.77-fold increase in the ratio of JC-1 aggregates to monomer compared to the Mn treatment (Fig. 5C and E). ATP level also elevated 1.48-fold in UA-pretreated BV2 cells compared to Mn-treated group (Fig. 5F). These findings indicated that microglial mitophagy suppression and mitochondrial dysfunction due to excessive Mn exposure can be effectively mitigated by UA pretreatment.
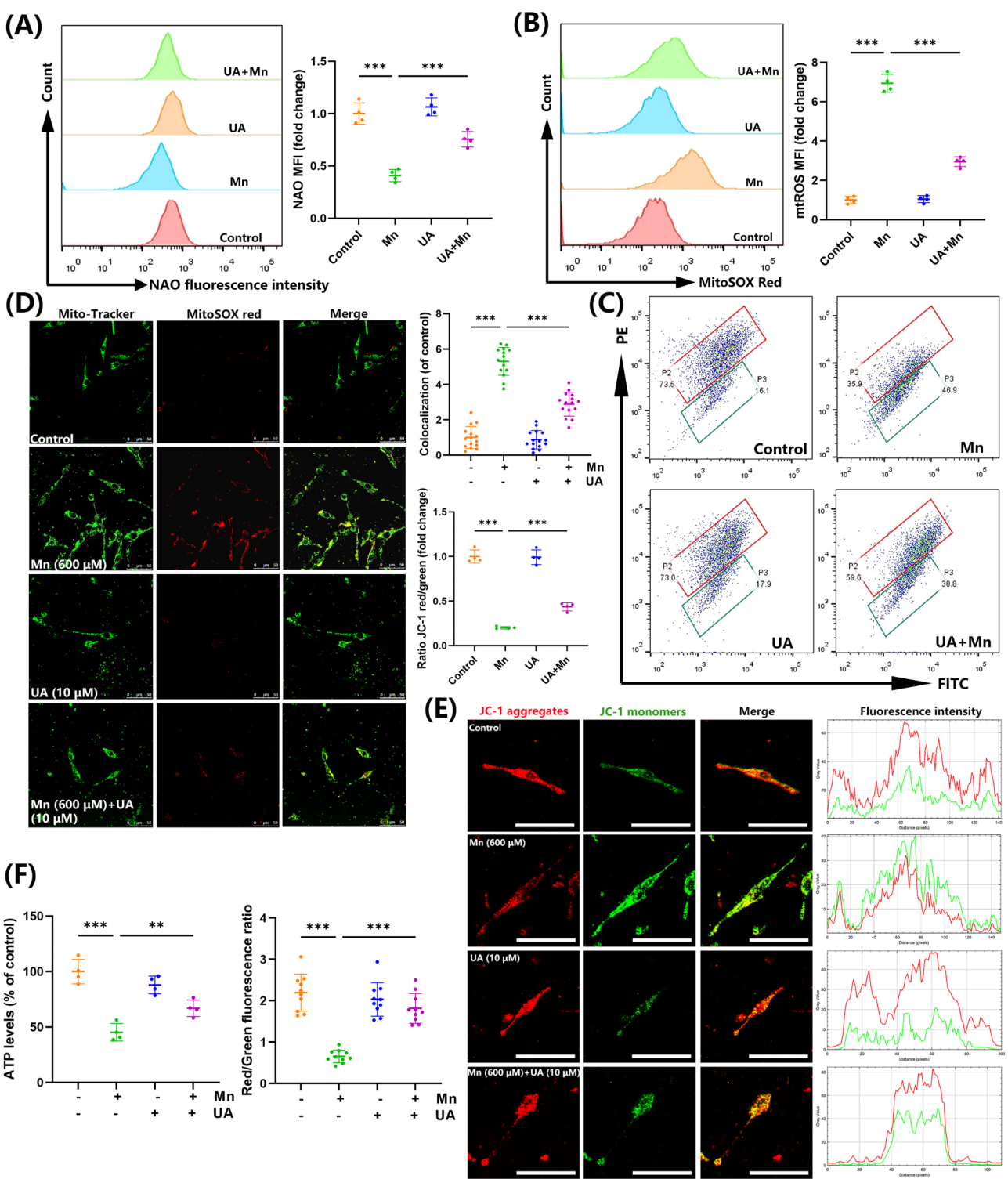
Fig. 5 UA pretreatment improved mitochondrial dysfunction induced by excessive Mn exposure. (**A**-**C**) Flow cytometry shows reduced mtROS, elevated mitochondrial mass, and MMP levels in the striatal after UA pretreatment compared with Mn-treated mice ($n = 4$ mice). (**D**, **E**) Immunofluorometric analysis reveals reduced mtROS and elevated MMP after UA pretreatment compared with Mn-treated BV2 cells ($n = 3$ independent experiments). (**F**) ATP levels increased after UA pretreatment compared with Mn-treated BV2 cells ($n = 4$ independent experiments). Data are presented as mean $\pm$ SD; significance is denoted as $^{**}P < 0.01$, $^{***}P < 0.001$
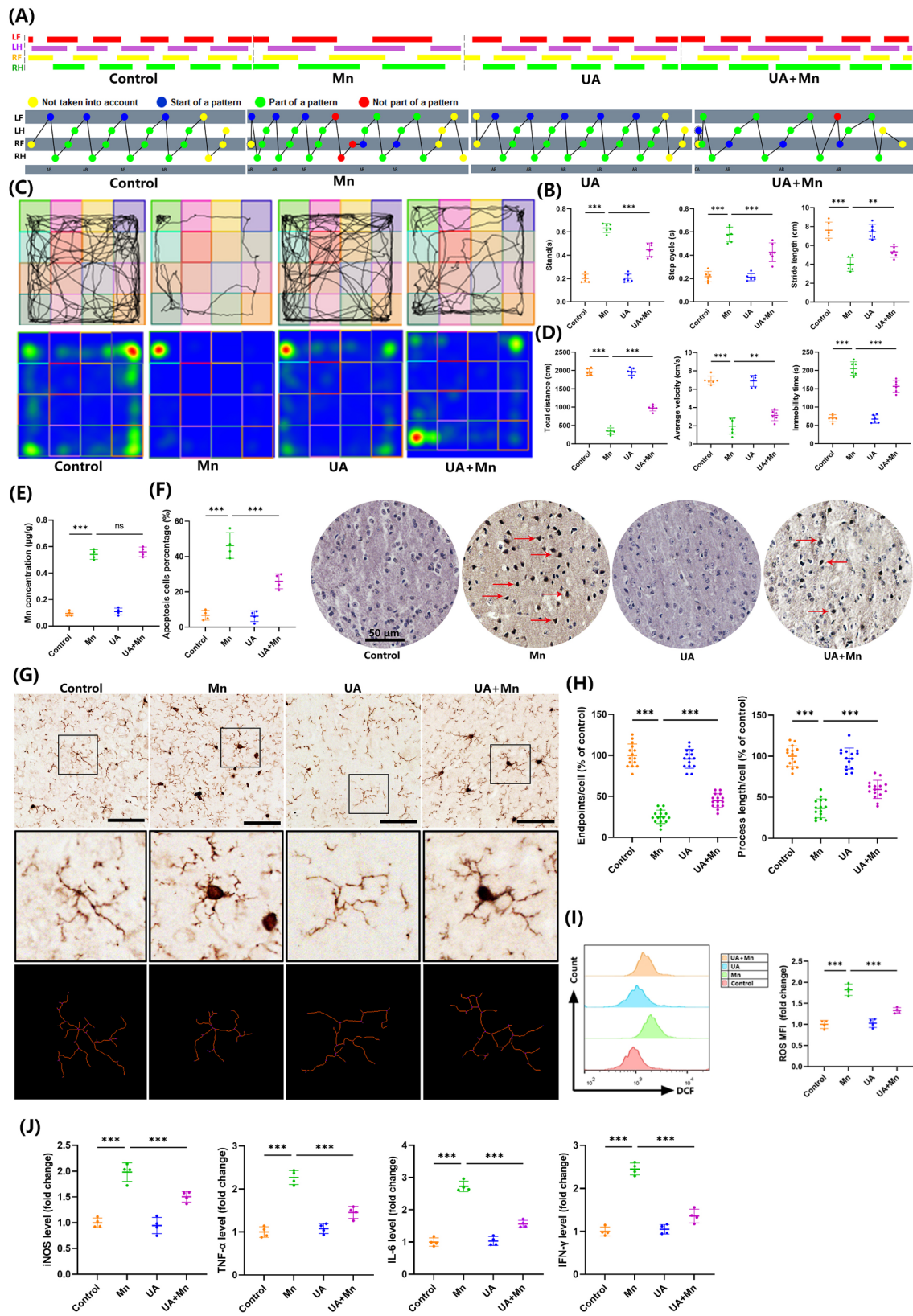
Fig. 6 (See legend on next page.)

(See figure on previous page.)

Fig. 6 UA pretreatment mitigated neurobehavioral deficits and aberrant microglial activation in Mn-treated mice. (**A**-**D**) Catwalk gait analysis and open-field test show elevated gait coordination performance and motor function levels in mice after UA pretreatment compared with Mn-treated ($n = 6$ mice). (**E**) Mn accumulation in the striatum was dose-dependent, and quantified by ICP-MS ($n = 4$ mice). (**F**) TUNEL assay demonstrates decreased nerve cell apoptosis after UA pretreatment compared with the Mn-treated group ($n = 4$ mice). (**G**, **H**) Iba-1 immunostaining reveals amoeboid microglial morphology after UA pretreatment compared with Mn-treated mice, with longer branches and more endpoints ($n = 3$ mice). (**I**) Flow cytometry shows reduced ROS levels in the striatum after UA pretreatment compared with Mn-treated ($n = 4$ mice). (**J**) ELISA results indicate decreased inflammatory cytokines (iNOS, TNF-α, IL-6, IFN-γ) in UA pretreatment compared with Mn-treated mice ($n = 4$ mice). Data are presented as mean ± SD; significance is denoted as $^*P < 0.05$, $^{**}P < 0.01$, $^{***}P < 0.001$

## UA pretreatment improves neurological function and reduces neuroinflammation in Mn-treated mice

The impact of UA pretreatment on Mn-induced neurological dysfunction was evaluated using open-field and catwalk gait analysis. UA-pretreated mice exhibited improved swinging cycles, step sequences, and motor coordination, which was manifested by a 29.5% reduction in stand time, a 26.4% decrease in step cycle, and a 1.3-fold increase in stride length compared to Mn-treated counterparts (Fig. 6A and B). Additionally, open-field test results showed a 2.8-fold increase in total distance, a 1.6-fold increase in average velocity, and a 23.7% decrease in immobility time in the UA pretreatment group compared to the Mn group (Fig. 6C and D). Mn accumulation in the striatum remained unchanged after UA pretreatment (Fig. 6E). The TUNEL assay showed 15% less nerve cell apoptosis in UA-pretreated group versus Mn-treated group (Fig. 6F). Immunohistochemistry demonstrated that UA pretreatment reduced amoeboid-like changes in Iba-1$^+$ microglia in Mn-treated mice, with a 1.1-fold increase in microglial branch endpoints and process length (Fig. 6G and H). Intracellular ROS levels were 27.0% lower in the UA pretreatment group compared to the Mn-treated group (Fig. 6I). Concomitantly, Mn-treated mice showed increased levels of inflammatory cytokines (iNOS, TNF-α, IL-6, and IFN-γ), which were significantly attenuated as a result of UA pretreatment (Fig. 6J). These data provide evidence for the upregulation of mitophagy by UA, which alleviates neurobehavioral impairments and reduces detrimental neuroinflammatory responses.

Upregulation of microglial mitophagy alleviated Mn-induced neuroinflammation by suppressing mtDNA-STING signaling pathways

To explore the underlying mechanisms by which mitophagy regulates microglia-mediated neuroinflammatory damage upon Mn overexposure, we extracted the striatum of the Mn-exposure mice to perform the single-nucleus RNA-sequencing (snRNA-seq) analysis. Uniform Manifold Approximation and Projection (UMAP) visualization analysis showed no observed different in major cell types (oligodendrocytes, neurons, microglia, and astrocytes) (Fig. 7A). In particular, we observed clear differences in the distribution density of microglia between Mn-treated mice and control mice (Fig. 7B-C). The results

of gene ontology (GO) and Kyoto Encyclopedia of Genes and Genomes (KEGG) pathway analysis showed that microglial differentially expressed genes (DEGs) in Mn-treated mice were associated with oxidative phosphorylation, Parkinson's disease, primary immunodeficiency, and other immune-related pathways (Fig. 7D). The top negatively enriched hallmark was oxidative phosphorylation signaling (Fig. 7E). Upon considering the significance of the cGAS-STING pathway in the cell's intrinsic immune defense, we speculated that its activation is probably involved in microglia-mediated neuroinflammation in the context of Mn neurotoxicity. We then interrogated our scRNA-seq dataset to determine whether the expression of the cGAS-STING signaling-related molecular genes (Cgas, Tmem173/Sting1, Tbk1, Irf3) was altered in the neuron and microglia subsets of Mn-treated mice and control mice. The activity of microglial cGAS-STING signaling was activated by excessive Mn exposure, while there were no observed changes in neurons (Fig. 7F). The transcript levels of microglial cGAS-STING signaling molecular genes were significantly increased in Mn-treated mice (Fig. 7G). A more refined analysis using Interferome showed that 30.3% of the significantly upregulated DEGs corresponded to interferon-stimulated genes (ISGs) (Fig. 7H). To corroborate these findings, we assessed changes in STING and its downstream molecule activity in BV2 cells following Mn or UA pretreatment. In line with the transcript data, there was a notable increase in the protein levels of p-STING/STING, p-TBK1/TBK1, and p-IRF3/IRF3 after Mn treatment, indicating activation of the cGAS-STING signaling pathway. However, this activation was mitigated by UA pretreatment (Fig. 8A). The cGAS-STING axis serves as a crucial sensor and downstream effector of mtDNA release-triggered inflammation. Anti-DNA immunostaining assay revealed a significant inhibiting effect of UA pretreatment on the increase in the amount of cytosolic DNA in Mn-treated BV2 cells (Fig. 8B). A qPCR assay revealed a 3.8-fold rise in mtDNA levels in Mn-treated BV2 cells compared to the control group. UA pretreatment resulted in a 48.1% reduction in mtDNA levels in BV2 cells compared to the Mn treatment group (Fig. 8C). These results suggested that the engagement of mitophagy in Mn-induced neuroinflammatory damage might be mediated by mtDNA-STING signaling.
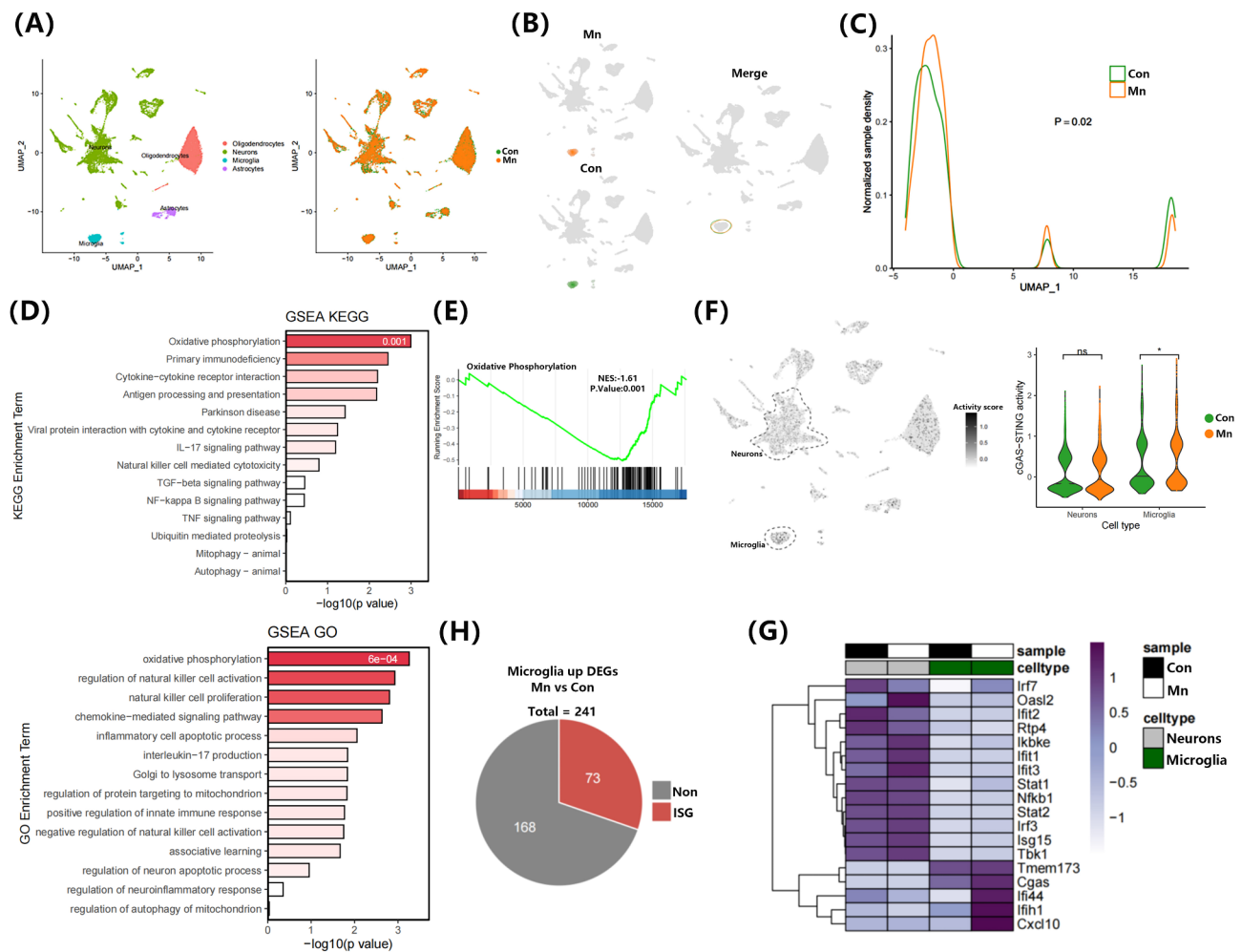
Fig. 7 Microglial cGAS-STING signaling was associated with Mn-induced mitochondrial dysfunction and neuroinflammatory response. (**A**) Representative integrated Uniform Manifold Approximation and Projection (UMAP) projection of snRNA-seq data, with clustering identification in Mn-treated mice and control mice. (**B**) The UMAP space indicates the same distribution of microglia from Mn-treated and control mice. (**C**) The continuous probability density curves of microglia clusters in Mn-treated mice and control mice were shown, scaled by sample. (**D**) scRNA-seq data showing the top enriched KEGG and GO pathways in microglial DEGs from Mn-treated mice and control mice. (**E**) Oxidative phosphorylation signaling was identified as the top negatively enriched hallmark in microglia of Mn-treated mice. (**F**) The heatmap and violin plots show cGAS-STING activity in neurons and microglia from Mn-treated mice and control mice. (**G**) Heatmap showing expression levels of cGAS-STING pathway modulators in neurons and microglia from Mn-treated mice and control mice. (**H**) Interferome analysis of upregulated microglial DEGs in Mn-treated mice, showing the proportion of interferon-stimulated genes (ISG, 30.3%). $n = 1$ mice in each group

Discussion

Studies have revealed the association of excessive Mn exposure with the onset of adverse health conditions, including neuromuscular diseases, such as Parkinson's disease and dystonia [4, 7–9, 11, 14, 56]. Microglia-mediated neuroinflammation plays a critical role in the development and progression of PD [19, 23, 57, 58]. Defective mitochondria in the microglia contribute to neuroinflammation and neurodegeneration through a variety of deleterious cellular pathways [1, 19, 20, 27, 33, 59]. In our study, we found that excessive Mn exposure causes the suppression of microglial mitophagy, coupled with mitochondria dysfunction and a detrimental microglia-mediated neuroinflammatory response, resulting in nerve cell

damage and neurobehavioral impairment. Upregulation of mitophagy by UA effectively improved the microglial mitochondria function and reduced neuroinflammation in response to Mn overexposure by modulating the mtDNA-STING signaling pathway.

Neuroinflammation has been identified in clinical and experimental studies as a key pathological driver of numerous neurological diseases [57]. In 1988, McGeer et al. first reported the presence of highly reactive microglia with human leukocyte antigen-DR immunopositive in the brain tissue of PD patients postmortem, emphasizing the crucial role of microglia-mediated neuroinflammation in the development of PD [1]. In recent years, the connection between neuroinflammation and PD
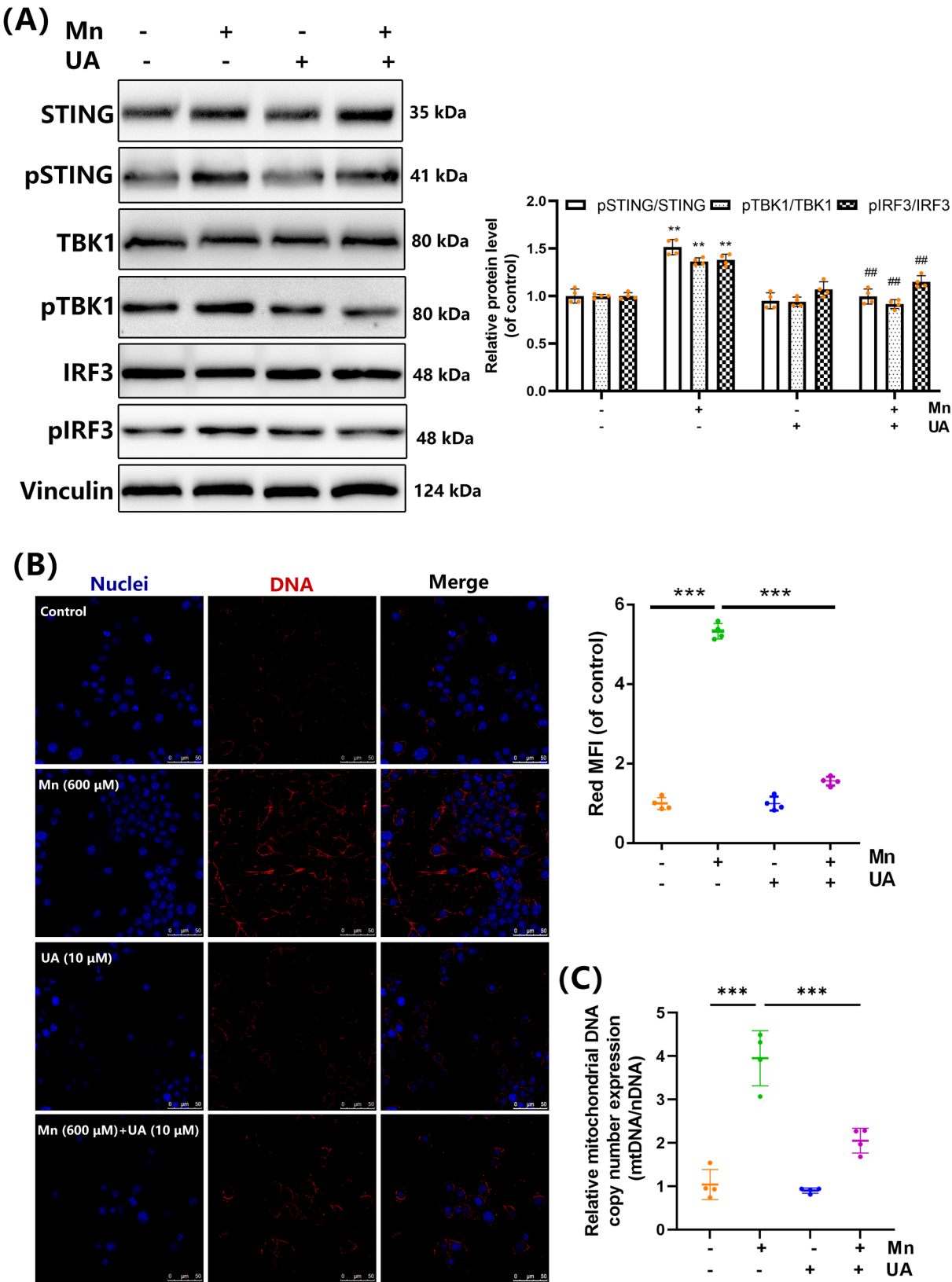
Fig. 8 (See legend on next page.)

(See figure on previous page.)

Fig. 8 UA pretreatment inhibited Mn-induced microglial mtDNA-STING activation. (**A**) Western blot analysis indicates STING signaling mediators (STING, pSTING, TBK1, pTBK1, IRF3, and pIRF3) dependent on mitophagy levels in UA-pretreated and Mn-treated BV2 cells. (**B**) Anti-DNA (red) immunostaining reveals decreased mtDNA in UA-pretreated compared with Mn-treated BV2 cells ($n=4$ independent experiments). (**C**) qPCR results indicate decreased cytosolic mtDNA in UA -pretreated compared with Mn-treated BV2 cells ($n=4$ independent experiments). Vinculin was used as a loading control. Data are presented as mean $\pm$ SD; significance is denoted as ***$P<0.001$, **$P<0.01$ vs. control group; ##$P<0.01$ vs. 600 μM Mn treated-BV2 cells group

has attracted widespread attention, with environmental exposure to Mn identified as a risk factor for PD, leading to dopaminergic neuronal loss and neuroinflammation [4, 6, 9, 17, 23, 25]. Excessive Mn exposure causes symptoms resembling PD, known as manganism. Notably, there are some distinctions in the pathological features between manganism and PD. For example, Lewy bodies, a hallmark of PD, do not form in manganism [12, 60]. Based on a dose translation formula, the 200 μmol/kg dose administered to Mn-exposed mice in this study is equivalent to 440 μg/kg bw/d in humans, a dosage similar to the observed Mn toxicity level in adults at 500 μg/d [61]. Microglia, the intrinsic immune cells of the brain, are pivotal in maintaining central nervous system (CNS) equilibrium by orchestrating immune responses. Upon stimulation or in the presence of disease, these cells transition from a quiescent state with a ramified morphology to an activated state characterized by morphological changes to an amoeboid shape and increased secretion of inflammatory mediators, including chemokines, cytokines, and interferons [19, 20, 57, 58]. In response to Mn-induced neurotoxicity, activation of microglia can result in the excessive production of ROS, along with inflammatory cytokines (TNF-α, IL-6, iNOS) [6]. In line with this, our initial findings revealed a progressive deterioration in neurobehavioral functions in mice with escalating Mn doses. Concurrently, there was a marked elevation in the Mn accumulation and intracellular ROS levels in the striatum of Mn-treated mice. Moreover, Mn exposure induced histopathological changes and adverse neuroinflammatory effects in the mice, manifesting as increased nerve cell apoptosis, amoeboid-like microglia with diminished branch length and number, and heightened levels of inflammatory cytokines (iNOS, TNF-α, IL-6, and IFN-γ). These findings imply that microglia-mediated neuroinflammation might be a predominant driver for Mn-induced parkinsonism, yet the molecular mechanisms involved remain unclear.

The activation and functional role of immune cells are influenced by their mitochondrial status. Recent findings indicate that microglial-mediated neuroinflammation plays a pivotal role in the pathophysiology of PD and is modulated by mitochondria. Various aspects of mitochondrial dysfunction, encompassing oxidative stress, respiratory chain restriction, inhibition of mitophagy, mitochondrial fragmentation, and disrupted mitochondrial homeostasis, all appear to be related to pro-inflammatory microglial activation [1, 20, 27, 33, 62]. In high

energy-demanding tissues such as the brain, the mitochondrial oxidative phosphorylation (OXPHOS) system generates ATP through the electron transport chain (ETC). Under conditions of damaged microglial mitochondria stress, there is a vicious cycle of excessive generation of mtROS and increased release of mtDNA into the cytosol. This process, frequently seen in PD, exacerbates mitochondrial dysfunction and inflammatory responses [1, 20, 59, 63]. Combined in vivo and in vitro, our studies found that Mn exposure triggers microglial mitochondrial function impairment. This specifically manifests as a progressive decrease in mitochondrial mass, a significant increase in mtROS, and a gradual decline in MMP and ATP levels in Mn-treated mice or BV2 cells. Our results indicate that targeting the regulation of microglial mitochondrial function could offer a promising avenue for managing Mn-induced neuroinflammatory damage.

Mitophagy serves as a pivotal machinery in maintaining mitochondrial quality control by degrading damaged mitochondria. This process is primarily mediated by the (PTEN-induced putative kinase 1) PINK1/Parkin pathway, where PINK1 recruits the E3 ubiquitin ligase Parkin to the outer mitochondrial membrane (OMM), leading to the phosphorylation of Parkin at Ser65. Parkin then ubiquitinates various OMM proteins, which are recognized by the autophagy receptor p62 and bound to lipidated microtubule-associated protein light chain 3/LC3II to form an autophagosome for degradation [35, 36]. Dysregulation of PINK1 and Parkin has been associated with Parkinson's disease (PD) [37]. Studies on Mn neurotoxicity have predominantly focused on neuronal damage resulting from mitochondrial dysfunction, including oxidative stress, mitochondria-dependent apoptotic cascade, inhibition of PINK1/Parkin-mediated mitophagy, respiratory inhibition, and mitochondrial fragmentation [6, 28–30]. Mice with loss-of-function mutations in PINK1 or Parkin exhibit increased inflammatory cytokine levels, underscoring the protective role of the PINK1/Parkin-mediated mitophagy pathway against inflammation [27, 37]. To investigate the impact of Mn-induced neuroinflammation on mitophagy, changes in mitophagy fluorescence signals (ATPB-mitochondria marker and LC3B-autophagy marker) were monitored, and the expression levels of mitophagy-related proteins (PINK1, Parkin, LC3B, p62) were assessed in current study. We found that the activity of mitophagy transitions from enhancement to suppression with increasing exposure to Mn. This transition is manifested by an increase

Lu *et al. Journal of Neuroinflammation*   (2025) 22:55

Page 18 of 20

in the correlation between ATPB and LC3B, upregulation of LC3-II, PINK1, and p-Parkin/Parkin, and a decrease in p62 expression at low and middle Mn doses in vivo and in vitro. Conversely, opposite effects are present in high-dose Mn treatment. These results suggest a crucial role of microglial mitophagy in modulating mitochondrial dysfunction and microglia-mediated neuroinflammation in response to excessive Mn exposure. This hypothesis was subsequently validated through the application of the mitophagy activator UA. Urolithin A (UA) is a bacterial metabolite produced by gut microbiota from ingested ellagitannins and ellagic acid, compounds found in various foods like pomegranate, raspberries, and nuts. This active metabolite has the ability to cross the blood-brain barrier and exhibits neuroprotective effects in models of Alzheimer's disease (AD), Parkinson's disease (PD), aging, and other brain injuries by promoting mitophagy, reducing inflammation, counteracting oxidative stress, and preventing cell death [44, 54, 55]. The dosage of UA used in our in vivo and in vitro experiments was determined based on previous studies that demonstrated significant enhancements in mitophagy and reductions in neuroinflammation, with no reported adverse effects [41, 45]. Our results consistently demonstrated amelioration of excessive Mn-induced mitophagy suppression and mitochondrial dysfunction following UA pretreatment in both mice and BV2 cells. Furthermore, UA-pretreated mice displayed improved neurobehavioral performance, reduced nerve cell apoptosis, attenuated microglial activation, and decreased levels of cellular ROS and proinflammatory cytokines (iNOS, TNF-α, IL-6, and IFN-γ) upon Mn overexposure. These findings suggest that excessive Mn-induced mitophagy suppression is implicated in microglia-mediated neuroinflammation.

To explore the potential molecular mechanism of microglial mitophagy regulating Mn-induced neuroinflammation, snRNA-seq was conducted to identify the distinct types of cell clusters and analyze the differential gene expression (DEGs) between Mn-treated mice and control mice. We found that Mn exposure increased the distribution density of microglia, whilst microglial DEGs focused on the oxidative phosphorylation, primary immunodeficiency, and other immune-related signaling. Considering mitochondria as an important work-site for OXPHOS, this result reflects the mitochondrial dysfunction induced by Mn. The cyclic GMP-AMP synthase (cGAS)-stimulator of interferon genes (STING) pathway is a pivotal machinery for driving innate immune responses by sensing cytosolic DNA stimuli. Upon encountering cytoplasmic DNA stress, cGAS synthesizes the second messenger 2'3'-cGAMP, which binds to and activates STING. Subsequently, STING is phosphorylated by TANK-binding kinase 1 (TBK1), facilitating the recruitment of TBK1 substrate interferon regulatory factor 3 (IRF3). This recruitment leads to IRF3 phosphorylation and dimerization. The homodimer then translocates to the nucleus and promotes the transcription of genes encoding type I IFNs and other pro-inflammatory factors [53, 64–67]. Abnormalities in the regulation of the cGAS-STING pathway has been implicated in the pathogenesis of neurodegenerative diseases, such as PD, AD, and amyotrophic lateral sclerosis. Recently, a novel discovery about Mn's capacity to regulate innate immunity as a good adjuvant in terms of antitumor and antivirus through activating the cGAS-STING pathway has been found [26, 38, 39]. However, excessive Mn exposure induced neuroinflammation by activating the microglial cGAS-STING pathway, resulting in neurodegeneration and cognitive impairment [22]. Upon sn-RNA sequencing analysis, it was evident that Mn exposure led to a marked enhancement in microglial cGAS-STING activity and an upregulation of ISG expression in mice. Uniformly, we also found a marked increase in the ratio of p-STING/STING, p-TBK1/TBK1, and p-IRF3/IRF3 protein expression was present in the Mn-treated BV2 cells. Conversely, this increase was mitigated by UA pretreatment. mtDNA is considered a key driver for cGAS-STING signaling activation, with mitochondrial dysfunction being a pathological hallmark of neurodegenerative disorders [27, 59, 64, 66, 68]. We hypothesized that excessive Mn exposure triggered the STING signaling activation due to the mtDNA released from damaged mitochondria into the cytosol. As expected, a notable increase in mtDNA levels was detected in Mn-treated BV2 cells, and yet a drastic reduction was observed after UA pretreatment. These results indicate that upregulation of microglial mitophagy by UA can reduce Mn-induced neuroinflammatory damage through the mtDNA-STING signaling pathway, providing a promising avenue for the treatment of Mn-induced neurotoxicity.

Conclusion

In summary, our study has elucidated the relationship between microglial mitophagy and Mn-induced neuroinflammatory damage, both in in vivo and in vitro models. Specifically, excessive Mn exposure suppresses microglial mitophagy, leading to mitochondrial dysfunction and neuroinflammatory damage. Mechanistically, we have unveiled the engagement of the microglial mtDNA-STING signaling pathway, which is modulated by mitophagy, in Mn-induced neuroinflammatory damage. These findings propose a compelling and original strategy for addressing Mn-induced neurological deficits.

Supplementary Information

Supplementary Material 1

Supplementary Material 2

Data availability
No datasets were generated or analysed during the current study.

Declarations

Competing interests
The authors declare no competing interests.

Conflict of interest
The authors declare that they have no conflict of interest.

Ethical approval
All experiments were conducted in compliance with the institutional guidelines for the care and use of laboratory animals in Jinzhou Medical University and the Regulations for the Administration of Affairs Concerning Experimental Animals of China. This study was approved by the Animal Research Committee at Jinzhou Medical University (IACUC Issue Number: 240079).

Author details
[1]School of Public Health, Jinzhou Medical University, Section III, Linghe District, Jinzhou, China
[2]Collaborative Innovation Center For Health Promotion of Children and Adolescents of Jinzhou Medical University, Jinzhou, China

References
1. Rajan S, Tryphena KP, Khan S, Vora L, Srivastava S, Singh SB et al. Understanding the involvement of innate immunity and the Nrf2-NLRP3 axis on mitochondrial health in Parkinson's disease. Ageing Res Rev. 2023;87(101915).
2. Morris HR, Spillantini MG, Sue CM, Williams-Gray CH. The pathogenesis of Parkinson's disease. Lancet (London England). 2024;403(10423):293–304.
3. Ben-Shlomo Y, Darweesh S, Llibre-Guerra J, Marras C, San Luciano M, Tanner C. The epidemiology of Parkinson's disease. Lancet (London England). 2024;403(10423):283–92.
4. Guilarte TR. Manganese and Parkinson's disease: a critical review and new findings. Environ Health Perspect. 2010;118(8):1071–80.
5. Palacios N, Fitzgerald K, Roberts AL, Hart JE, Weisskopf MG, Schwarzschild MA, et al. A prospective analysis of airborne metal exposures and risk of Parkinson disease in the nurses' health study cohort. Environ Health Perspect. 2014;122(9):933–8.
6. Harischandra DS, Ghaisas S, Zenitsky G, Jin H, Kanthasamy A, Anantharam V, et al. Manganese-Induced neurotoxicity: new insights into the triad of protein misfolding, mitochondrial impairment, and neuroinflammation. Front Neurosci. 2019;13:654.
7. Wen Y, Fu Z, Li J, Liu M, Wang X, Chen J et al. Targeting m6A mRNA demethylase FTO alleviates manganese-induced cognitive memory deficits in mice. J Hazard Mater. 2024;476(134969).
8. Wei S, Ma X, Liang G, He J, Wang J, Chen H et al. The role of circHmbox1(3,4) in ferroptosis-mediated cognitive impairments induced by manganese. J Hazard Mater. 2024;476(135212).
9. Huang Q, Wan J, Nan W, Li S, He B, Peng Z. Association between manganese exposure in heavy metals mixtures and the prevalence of sarcopenia in US adults from NHANES 2011–2018. J Hazard Mater. 2024;464(133005).
10. Bi Y, Huang N, Xu D, Wu S, Meng Q, Chen H et al. Manganese exposure leads to depressive-like behavior through disruption of the Gln-Glu-GABA metabolic cycle. J Hazard Mater. 2024;480(135808).
11. Lu M, Deng P, Yang L, Wang X, Mei X, Zhou C et al. Manganese overexposure induces Parkinson-like symptoms, altered lipid signature and oxidative stress in C57BL/6 J mouse. Ecotoxicol Environ Saf. 2023;263(115238).
12. Peres TV, Schettinger MRC, Chen P, Carvalho F, Avila DS, Bowman AB, et al. Manganese-induced neurotoxicity: a review of its behavioral consequences and neuroprotective strategies. BMC Pharmacol Toxicol. 2016;17(1):57.
13. Das K, Waiba S, Jana A, Maji B. Manganese-catalyzed hydrogenation, dehydrogenation, and hydroelementation reactions. Chem Soc Rev. 2022;51(11):4386–464.
14. Kim H, Harrison FE, Aschner M, Bowman AB. Exposing the role of metals in neurological disorders: a focus on manganese. Trends Mol Med. 2022;28(7):555–68.
15. Dos Anjos Cordeiro JM, Santos LC, Santos BR, de Jesus Nascimento AE, Santos EO, Barbosa EM et al. Manganese porphyrin-based treatment improves fetal-placental development and protects against oxidative damage and NLRP3 inflammasome activation in a rat maternal hypothyroidism model. Redox Biol. 2024;74(103238).
16. Balachandran RC, Mukhopadhyay S, McBride D, Veevers J, Harrison FE, Aschner M, et al. Brain manganese and the balance between essential roles and neurotoxicity. J Biol Chem. 2020;295(19):6312–29.
17. Budinger D, Barral S, Soo AKS, Kurian MA. The role of manganese dysregulation in neurological disease: emerging evidence. The lancet. Neurology. 2021;20(11):956–68.
18. Nyarko-Danquah I, Pajarillo E, Digman A, Soliman KFA, Aschner M, Lee E. Manganese accumulation in the brain via various transporters and its neurotoxicity mechanisms. Molecules. 2020;25(24).
19. Quick JD, Silva C, Wong JH, Lim KL, Reynolds R, Barron AM, et al. Lysosomal acidification dysfunction in microglia: an emerging pathogenic mechanism of neuroinflammation and neurodegeneration. J Neuroinflammation. 2023;20(1):185.
20. Peruzzotti-Jametti L, Willis CM, Krzak G, Hamel R, Pirvan L, Ionescu RB, et al. Mitochondrial complex I activity in microglia sustains neuroinflammation. Nature. 2024;628(8006):195–203.
21. Wang D, Zhang J, Jiang W, Cao Z, Zhao F, Cai T, et al. The role of NLRP3-CASP1 in inflammasome-mediated neuroinflammation and autophagy dysfunction in manganese-induced, hippocampal-dependent impairment of learning and memory ability. Autophagy. 2017;13(5):914–27.
22. Wu J, Chen H, Guo T, Li M, Yang C, Aschner M et al. Sesamol alleviates manganese-induced neuroinflammation and cognitive impairment via regulating the microglial cGAS-STING/NF-κB pathway. Environ Pollut. 2022;120988.
23. Yan D, Yang Y, Lang J, Wang X, Huang Y, Meng J et al. SIRT1/FOXO3-mediated autophagy signaling involved in manganese-induced neuroinflammation in microglia. Ecotoxicol Environ Saf. 2023;256(114872).
24. Tinkov AA, Paoliello MMB, Mazilina AN, Skalny AV, Martins AC, Voskresenskaya ON et al. Molecular targets of Manganese-Induced neurotoxicity: A Five-Year update. Int J Mol Sci. 2021;22(9).
25. Pajarillo E, Kim S, Digman A, Dutton M, Son D-S, Aschner M, et al. The role of microglial LRRK2 kinase in manganese-induced inflammatory neurotoxicity via NLRP3 inflammasome and RAB10-mediated autophagy dysfunction. J Biol Chem. 2023;299(7):104879.
26. Zhang R, Wang C, Guan Y, Wei X, Sha M, Yi M, et al. Manganese salts function as potent adjuvants. Cell Mol Immunol. 2021;18(5):1222–34.
27. Stolz A, Dikic I. Elusive mitochondrial connection to inflammation uncovered. Nature. 2018;561(7722):185–6.
28. Liu K, Liu Z, Liu Z, Ma Z, Jia Y, Deng Y et al. Manganese-induced PINK1 S-nitrosylation exacerbates nerve cell damage by promoting ZNF746 repression of mitochondrial biogenesis. Sci Total Environ. 2023;863(160985).

29. Lei MY, Cong L, Liu ZQ, Liu ZF, Ma Z, Liu K, et al. Resveratrol reduces DRP1-mediated mitochondrial dysfunction via the SIRT1-PGC1α signaling pathway in manganese-induced nerve damage in mice. Environ Toxicol. 2022;37(2):282–98.

30. Liu K, Liu Z, Liu Z, Ma Z, Deng Y, Liu W et al. Manganese induces S-nitrosylation of PINK1 leading to nerve cell damage by repressing PINK1/Parkin-mediated mitophagy. Sci Total Environ. 2022;834(155358).

31. Burbulla LF, Song P, Mazzulli JR, Zampese E, Wong YC, Jeon S, et al. Dopamine oxidation mediates mitochondrial and lysosomal dysfunction in Parkinson's disease. Science. 2017;357(6357):1255–61.

32. Kim S, Wong YC, Gao F, Krainc D. Dysregulation of mitochondria-lysosome contacts by GBA1 dysfunction in dopaminergic neuronal models of Parkinson's disease. Nat Commun. 2021;12(1):1807.

33. Lawrence GMEP, Holley CL, Schroder K. Parkinson's disease: connecting mitochondria to inflammasomes. Trends Immunol. 2022;43(11):877–85.

34. Ashleigh T, Swerdlow RH, Beal MF. The role of mitochondrial dysfunction in Alzheimer's disease pathogenesis. Alzheimer's Dement J Alzheimer's Assoc. 2023;19(1):333–42.

35. D'Arcy MS. Mitophagy in health and disease. Molecular mechanisms, regulatory pathways, and therapeutic implications. Apoptosis. 2024;29(9–10):1415–28.

36. Wang S, Long H, Hou L, Feng B, Ma Z, Wu Y, et al. The mitophagy pathway and its implications in human diseases. Signal Transduct Target Ther. 2023;8(1):304.

37. Sliter DA, Martinez J, Hao L, Chen X, Sun N, Fischer TD, et al. Parkin and PINK1 mitigate STING-induced inflammation. Nature. 2018;561(7722):258–62.

38. Lv M, Chen M, Zhang R, Zhang W, Wang C, Zhang Y, et al. Manganese is critical for antitumor immune responses via cGAS-STING and improves the efficacy of clinical immunotherapy. Cell Res. 2020;30(11):966–79.

39. Wang C, Guan Y, Lv M, Zhang R, Guo Z, Wei X et al. Manganese increases the sensitivity of the cGAS-STING pathway for Double-Stranded DNA and is required for the host defense against DNA viruses. Immunity. 2018;48(4).

40. Sun X, Zhang Y, Li J, Park KS, Han K, Zhou X, et al. Amplifying STING activation by Cyclic dinucleotide-manganese particles for local and systemic cancer metalloimmunotherapy. Nat Nanotechnol. 2021;16(11):1260–70.

41. Jiménez-Loygorri JA-O, Villarejo-Zori B, Viedma-Poyatos Á, Zapata-Muñoz J, Benítez-Fernández RA-O, Frutos-Lisón MD, et al. Mitophagy curtails cytosolic mtDNA-dependent activation of cGAS/STING inflammation during aging. Nat Commun. 2024;15(1):830. (2041– 1723 (Electronic)).

42. Ma Z, Wang C, Liu C, Yan DY, Tan X, Liu K et al. Manganese induces autophagy dysregulation: the role of S-nitrosylation in regulating autophagy related proteins in vivo and in vitro. Sci Total Environ. 2020;698(134294).

43. Yan DY, Liu C, Tan X, Ma Z, Wang C, Deng Y, et al. Mn-Induced neurocytes injury and autophagy dysfunction in Alpha-Synuclein Wild-Type and Knock-Out mice: highlighting the role of Alpha-Synuclein. Neurotox Res. 2019;36(1):66–80.

44. Wojciechowska O, Kujawska M, Urolithin. A in Health and Diseases: Prospects for Parkinson's Disease Management. Antioxid (Basel). 2023;12(7).

45. Qiu J, Chen Y, Zhuo J, Zhang L, Liu J, Wang B et al. Urolithin A promotes mitophagy and suppresses NLRP3 inflammasome activation in lipopolysaccharide-induced BV2 microglial cells and MPTP-induced Parkinson's disease model. Neuropharmacology. 2022;207(108963).

46. Hao Y, Hao S, Andersen-Nissen E, Mauck WM, Zheng S, Butler A et al. Integrated analysis of multimodal single-cell data. Cell. 2021;184(13).

47. McGinnis CS, Murrow LM, Gartner ZJ, DoubletFinder. Doublet detection in Single-Cell RNA sequencing data using artificial nearest neighbors. Cell Syst. 2019;8(4).

48. Korsunsky I, Millard N, Fan J, Slowikowski K, Zhang F, Wei K, et al. Fast, sensitive and accurate integration of single-cell data with harmony. Nat Methods. 2019;16(12):1289–96.

49. Aran D, Looney AP, Liu L, Wu E, Fong V, Hsu A, et al. Reference-based analysis of lung single-cell sequencing reveals a transitional profibrotic macrophage. Nat Immunol. 2019;20(2):163–72.

50. Wu T, Hu E, Xu S, Chen M, Guo P, Dai Z, et al. ClusterProfiler 4.0: A universal enrichment tool for interpreting omics data. Innov (Camb). 2021;2(3):100141.

51. Alvarez MJ, Shen Y, Giorgi FM, Lachmann A, Ding BB, Ye BH, et al. Functional characterization of somatic mutations in cancer using network-based inference of protein activity. Nat Genet. 2016;48(8):838–47.

52. Rusinova I, Forster S, Yu S, Kannan A, Masse M, Cumming H, et al. Interferome v2.0: an updated database of annotated interferon-regulated genes. Nucleic Acids Res. 2013;41(Database issue):D1040–6.

53. Jiménez-Loygorri JI, Boya P. Aging STINGs: mitophagy at the crossroads of neuroinflammation. Autophagy. 2024;20(7):1684–6.

54. D'Amico D, Andreux PA, Valdés P, Singh A, Rinsch C, Auwerx J. Impact of the natural compound urolithin A on health, disease, and aging. Trends Mol Med. 2021;27(7):687–99.

55. Kuerec AH, Lim XK, Khoo AL, Sandalova E, Guan L, Feng L et al. Targeting aging with urolithin A in humans: A systematic review. Ageing Res Rev. 2024;100(102406).

56. Qi Z, Wang S, Li J, Wen Y, Cui R, Zhang K et al. Protective role of mRNA demethylase FTO on axon guidance molecules of nigro-striatal projection system in manganese-induced parkinsonism. J Hazard Mater. 2022;426(128099).

57. Silvin A, Uderhardt S, Piot C, Da Mesquita S, Yang K, Geirsdottir L et al. Dual ontogeny of disease-associated microglia and disease inflammatory macrophages in aging and neurodegeneration. Immunity. 2022;55(8).

58. Zhu R, Luo Y, Li S, Wang Z. The role of microglial autophagy in Parkinson's disease. Front Aging Neurosci. 2022;14(1039780).

59. Riley JS, Tait SW. Mitochondrial DNA in inflammation and immunity. EMBO Rep. 2020;21(4):e49799.

60. O'Neal SL, Zheng W. Manganese toxicity upon overexposure: a decade in review. Curr Environ Health Rep. 2015;2(3):315–28.

61. Yan D, Gao L, Lang J, Gao X, Ma H. Effects of manganese on microglia M1/M2 polarization and SIRT1-mediated transcription of STAT3-dependent genes in mouse. Environ Toxicol. 2021;36(9):1729–41.

62. Spinelli JB, Haigis MC. The multifaceted contributions of mitochondria to cellular metabolism. Nat Cell Biol. 2018;20(7):745–54.

63. Collier JJ, Oláhová M, McWilliams TG, Taylor RW. Mitochondrial signalling and homeostasis: from cell biology to neurological disease. Trends Neurosci. 2023;46(2):137–52.

64. Chung KW, Dhillon P, Huang S, Sheng X, Shrestha R, Qiu C, et al. Mitochondrial damage and activation of the STING pathway lead to renal inflammation and fibrosis. Cell Metab. 2019;30(4):784–e799785.

65. Gulen MF, Samson N, Keller A, Schwabenland M, Liu C, Glück S, et al. cGAS-STING drives ageing-related inflammation and neurodegeneration. Nature. 2023;620(7973):374–80.

66. Kim J, Kim HS, Chung JH. Molecular mechanisms of mitochondrial DNA release and activation of the cGAS-STING pathway. Exp Mol Med. 2023;55(3):510–9.

67. Zhang X, Liu J, Wang H. The cGAS-STING-autophagy pathway: novel perspectives in neurotoxicity induced by manganese exposure. Environ Pollut. 2022;315(120412).

68. Newman LE, Weiser Novak S, Rojas GR, Tadepalle N, Schiavon CR, Grotjahn DA, et al. Mitochondrial DNA replication stress triggers a pro-inflammatory endosomal pathway of nucleoid disposal. Nat Cell Biol. 2024;26(2):194–206.

Publisher's note